CHAPTER IV
RESULTS AND DISCUSSIONS

4.1 Nanocellulose analysis

4.1.1 Nanocellulose characterization

Characterization of the dried cellulose revealed a primary composition of cellulose fibers with a lignin content of 0.53% and a hemicellulose content of 6.63%, as determined through chemical analysis. Field emission scanning electron microscopy (FESEM) was employed to investigate the cellulose morphology, which is presented in Figure 4.1.

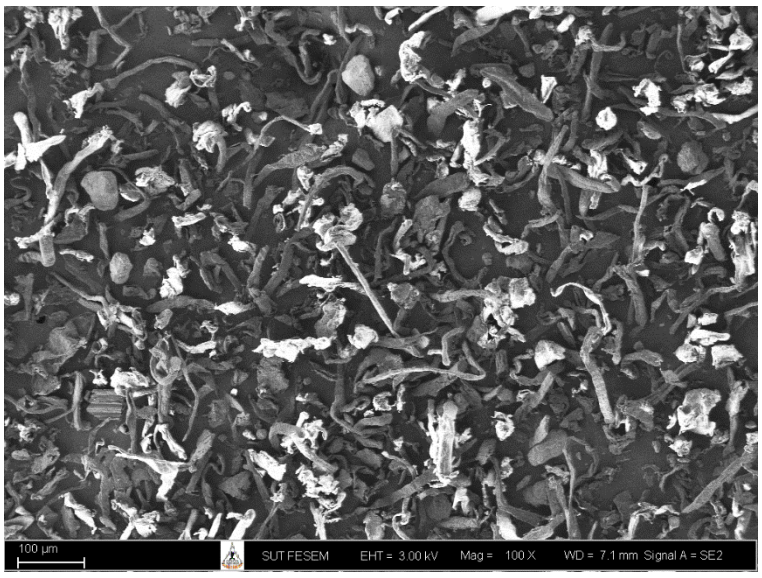

Figure 4.1 FESEM image of sieved cellulose.

The initial cellulose mixture possessed an average particle size of 43 µm before undergoing high-pressure homogenization. All three samples, the homogenized mixture, the enzyme-treated product, and the nanocellulose powder depicted in Figure 4.2 were subjected to analysis to determine their average particle sizes (Figure 4.3). The optimal particle size reduction of 278.9 nm was achieved using high-pressure homogenization at 30,000 psi for 15 passes with the addition of a 7% enzyme cocktail. These findings suggest

that the enzyme cocktail played a substantial role in facilitating size reduction, with high-pressure homogenization further augmenting this effect.

The cellulose nanofibers (CNF) were examined in PBS for tissue engineering scaffolds and reported that CNFs with lengths of 500-800 nm and diameters below 50 nm resulted in the best combination of mechanical strength and cell attachment properties(Lin et al., 2011). In addition, biocompatibility aspects of nanocellulose were studied in various polymers and found that for biomedical implants, CNFs with aspect ratios (length/diameter) between 70-100 showed reduced inflammatory responses while maintaining mechanical advantages (Endes et al., 2016). The optimal size of nanocellulose for biomedical applications remains unclear. This is because nanocellulose size significantly influences the mechanical properties of the composite. However, the ideal size depends on the specific biomedical application and its intended purpose.

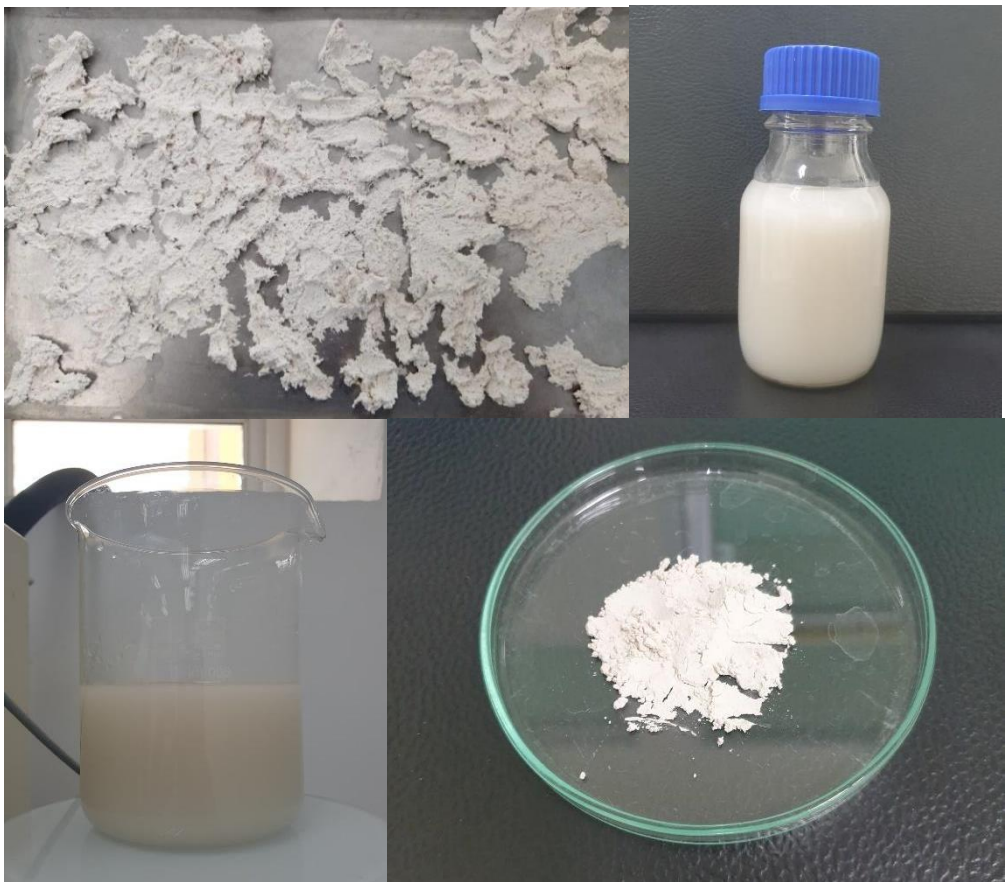

Figure 4.2 image of sample in nanocellulose preparation a) dried cellulose, b) homogenized cellulose mixture, c) enzyme-containing product (homogenized cellulose mixture was added by enzyme) and d) nanocellulose powder.

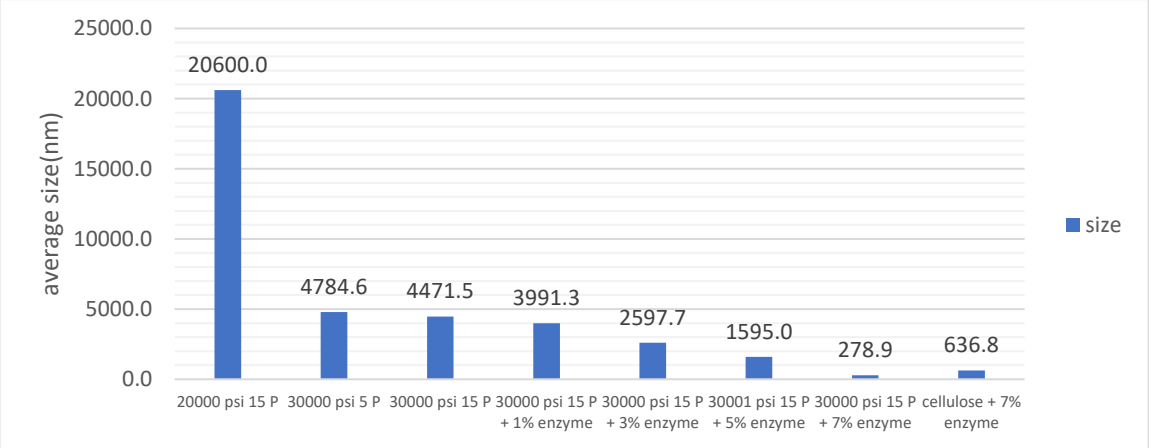

Figure 4.3 average size (nm) of nanocellulose with different conditions.

The polydispersity index (PDI) served as a metric to evaluate the distribution of particle sizes within the nanocellulose samples. The PDI values for nanocellulose produced under various processing conditions were presented in Table 4.1 The structural modifications induced by high-pressure homogenization were hypothesized to render the cellulose fibrils more amenable to enzymatic degradation during subsequent hydrolysis. This enhanced susceptibility to enzymatic hydrolysis can be attributed to the substantial shortening of the fibrils observed following enzymatic treatment. As a direct consequence, the incorporation of enzymes resulted in a significant elevation of the PDI of the nanocellulose. The enzyme cocktail functions synergistically, though each enzyme follows a distinct action pattern, further contributing to size heterogeneity. The increased PDI indicates a broader particle size distribution after enzymatic treatment. While the average particle size may decrease, the resulting population becomes more diverse, comprising both very small fragments from regions highly susceptible to enzymatic attack and larger fragments from more resistant regions.

Table 4.1 Polydispersity index (PDI) of nanocellulose with different conditions.

sample	PDI
20000 psi 15 P	0.554
30000 psi 5 P	0.390
30000 psi 15 P	0.462
30000 psi 15 P + 1% enzyme	0.567
30000 psi 15 P + 3% enzyme	0.616
30001 psi 15 P + 5% enzyme	0.669
30000 psi 15 P + 7% enzyme	0.752
cellulose + 7% enzyme	0.720

Zeta potential, a physicochemical property quantifying the electrostatic potential at the interface between a solid particle and a surrounding liquid, was presented for the nanocellulose samples in Figure 4.4 Intriguingly, the zeta potential of the nanocellulose exhibited a significant reduction to approximately -20 mV following high-pressure homogenization at 30,000 psi for 15 cycles. This observation suggests a pressure-dependent decline in zeta potential magnitude during homogenization. The observed decrease can potentially be attributed to the exposure of anionic functional groups on the nanocellulose surface. This phenomenon may result from cellulose fiber release or surface chemistry alterations induced by the mechanical stress of homogenization, as previously reported (Wu et al., 2020). Conversely, the enzymatic treatment is not recognized to introduce negatively charged groups onto the surface of the nanocellulose. Notably, materials with lower negative zeta potential values are generally considered more favorable for specific biomedical applications (Squinca et al., 2020).

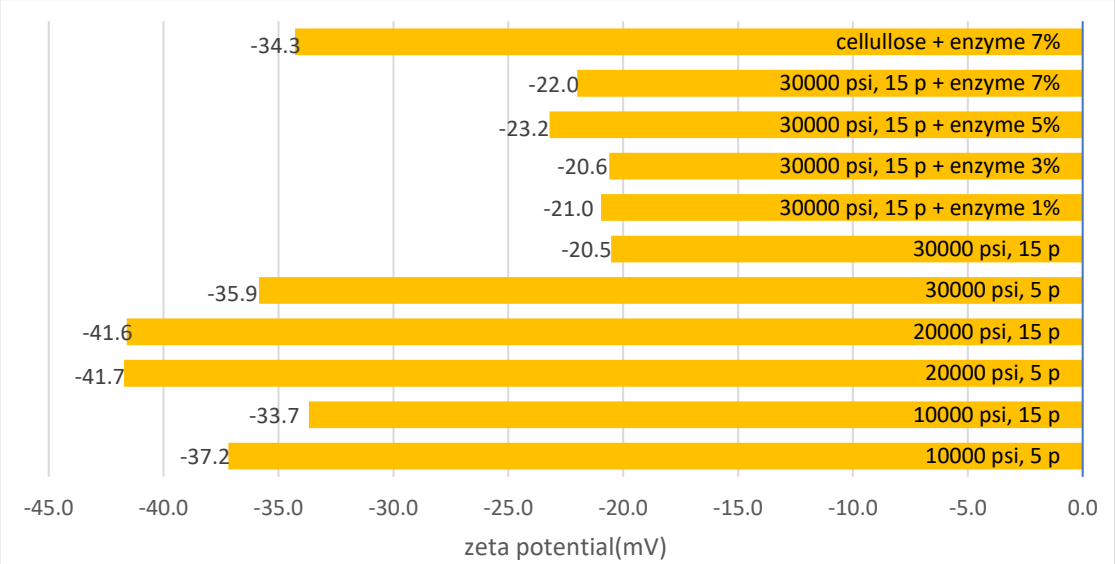

Figure 4.4 zeta potential (mV) of nanocellulose with different conditions.

4.1.2 Morphological analysis

The morphology of cellulose processed solely through mechanical means is illustrated in Figure 4.5(left) The image depicts extensive fibrillation, a consequence of high-pressure homogenization at 10,000 psi for 5 cycles. Conversely, Figure 4.5 (middle) provides a clear visualization of the nanocellulose obtained through the synergistic application of high-pressure homogenization and enzymatic hydrolysis. Notably, the nanocellulose exhibits a markedly reduced particle size compared to cellulose processed solely by the mechanical technique. The enzymatic hydrolysis was postulated to have instigated a cascade of complex reactions, ultimately transforming the cellulose fibril morphology into a more spherical configuration. Moreover, transmission electron microscopy (TEM) was utilized to examine the crystal structure of the nanocellulose derived from the combined methods, as presented in Figure 4.5 (right).

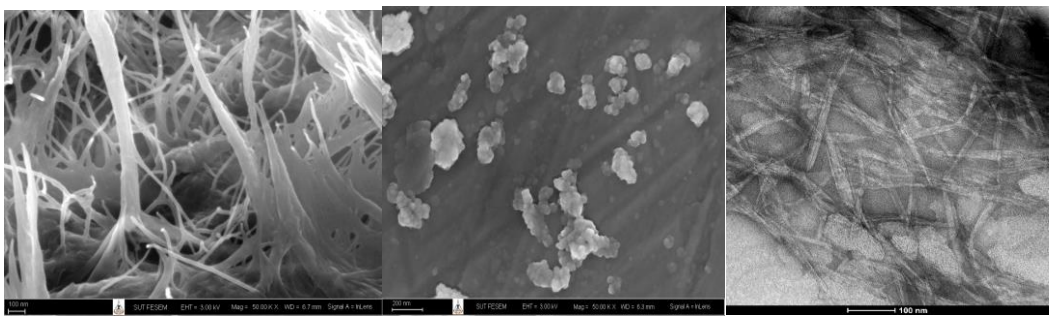

Figure 4.5 FESEM image of cellulose nanofibrils from high pressure homogenization at 10,000 psi 5 pass (left), FESEM image of nanocellulose from high pressure homogenization at 30,000 psi, 15 pass couple with enzymatic process (7% of enzyme) (middle), TEM image cellulose nanocrystal from high pressure homogenization at 30,000 psi, 15 pass couple with enzymatic process (7% of enzyme) (right)

4.1.3 FTIR analysis

Fourier Transform Infrared (FTIR) spectroscopy serves as a well-established analytical technique for elucidating the chemical functionalities and structural characteristics of cellulose. The average spectra obtained for nanocellulose processed under various conditions are presented in Figure 4.6.

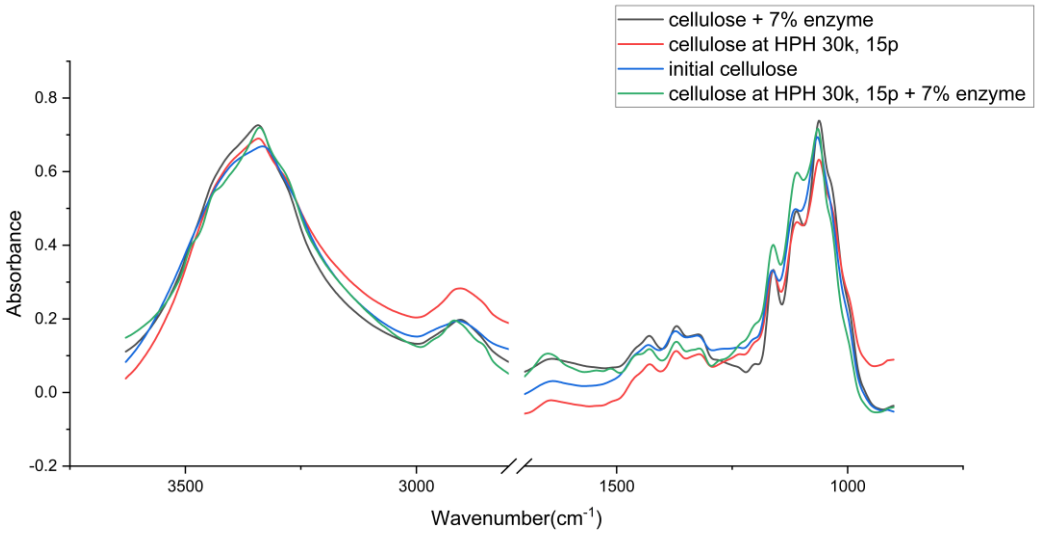

Figure 4.6 The original average FTIR spectra of nanocellulose in different conditions and initial cellulose in wavenumber ranges of 3630-2770 cm^{-1} and 1720-900 cm^{-1}.

Principal component analysis (PCA) represents a multivariate statistical method employed to analyze large datasets. In this study, PCA was utilized to characterize the FTIR spectra of the nanocellulose samples. Typically, PCA applied to spectroscopic data yields two primary types of information including. First, the expression of a group of similar spectra within the dataset was visualized in a scatter plot (Figure 4.7A). This 2D PCA score plot depicts PC-1 (contributing 30% of the variance) versus PC-2 (contributing 6% of the variance). The second type, the loadings corresponded to the influence of specific spectral features on the observed variation. These loadings were presented in Figure 4.7B. The negative loading plot was illustrated in Figure 4.7B (top), which relates to the positive score plot of the initial cellulose by PC-2 (represented by the blue symbol). The FTIR spectral bands were summarized in Table 4.2

Table 4.2 FTIR Spectral Bands and Assignments

Peak (cm^{-1})	Assignment	Reference
3490, 3442	Intramolecular OH (cellulose II)	[Hishikawa et al., 2017, Makarem et al., 2019]
3320	Intramolecular OH (cellulose)	[Hishikawa et al., 2017, Makarem et al., 2019]
3339	Intermolecular OH (cellulose Iα and Iβ)	[Hishikawa et al., 2017, Makarem et al., 2019]
3276	Intermolecular OH (cellulose Iβ)	[Hishikawa et al., 2017, Makarem et al., 2019]
2919	CH stretching vibration	[Hishikawa et al., 2017, Makarem et al., 2019]
2965	CH_2 asymmetric stretching (cellulose)	[Hishikawa et al., 2017, Makarem et al., 2019, Boukir et al.,2019]
2852	CH_2 symmetric stretching (cellulose)	[Hishikawa et al., 2017, Makarem et al., 2019, Boukir et al.,2019]
1511	Aromatic skeletal vibration (lignin)	[Javier-Astete et al., 2021, Salim et al., 2021]
1459, 1373, 1315	CH_2 bending vibration (crystalline cellulose I)	[Makarem et al., 2019, Boukir et al.,2019]
1425	CH_2 asymmetric stretching (amorphous cellulose)	[Makarem et al., 2019, Boukir et al.,2019]
1384	C-H (cellulose)	[Hishikawa et al., 2017, Makarem et al., 2019]

Peak (cm^{-1})	Assignment	Reference
1278	CH deformation (cellulose I and II)	[Makarem et al., 2019, Boukir et al.,2019, Salim et al., 2021]
1174, 1128	C-O-C (cellulose)	[Makarem et al., 2019, Boukir et al.,2019]
1162, 1120	C-O-C asymmetric stretching (cellulose I and II)	[Boukir et al.,2019, Salim et al., 2021, Kudzin et al., 2021]
1072, 1041, 1000	-C-O- (cellulose)	[Makarem et al., 2019, Boukir et al.,2019, Salim et al., 2021, Kudzin et al., 2021]
1062, 1029, 995	C-O vibration and C-O valence vibration (cellulose)	[Oudiani et al., 2017, Parihar et al., 2019]

The negative loadings at peaks 3320 cm^{-1} (intramolecular OH cellulose), 1384 cm^{-1} (C-H in cellulose), 1174 cm^{-1}, and 1128 cm^{-1} (C-O-C in cellulose), 1072 cm^{-1}, 1041 cm^{-1}, and 1000 cm^{-1} (-C-O- in cellulose) indicate a strong association of these wavenumbers with the initial cellulose structure. Conversely, the positive loading plot (Figure 4.7B, bottom) was associated with the negative score plot of the cellulose processed with high-pressure homogenization (HPH) at 30,000 psi for 15 cycles with the addition of 7% enzyme (represented by the green symbol) by PC-2. The positive loadings at peaks 3490 cm^{-1} and 3442 cm^{-1} (intramolecular OH cellulose), 3339 cm^{-1} (intermolecular OH cellulose), 2850 cm^{-1} and 1315 cm^{-1}(CH_2 in cellulose), and 1064 cm^{-1} (C-OH in cellulose) suggest a prominent contribution of these functionalities to the spectral variations observed in the HPH + enzyme treated cellulose. Additionally, the negative loadings at peaks 1064 cm^{-1}, 1020 cm-1, and 991 cm^{-1} (-C-O- in cellulose) imply potential structural modifications in these regions following the combined HPH and enzymatic treatment.

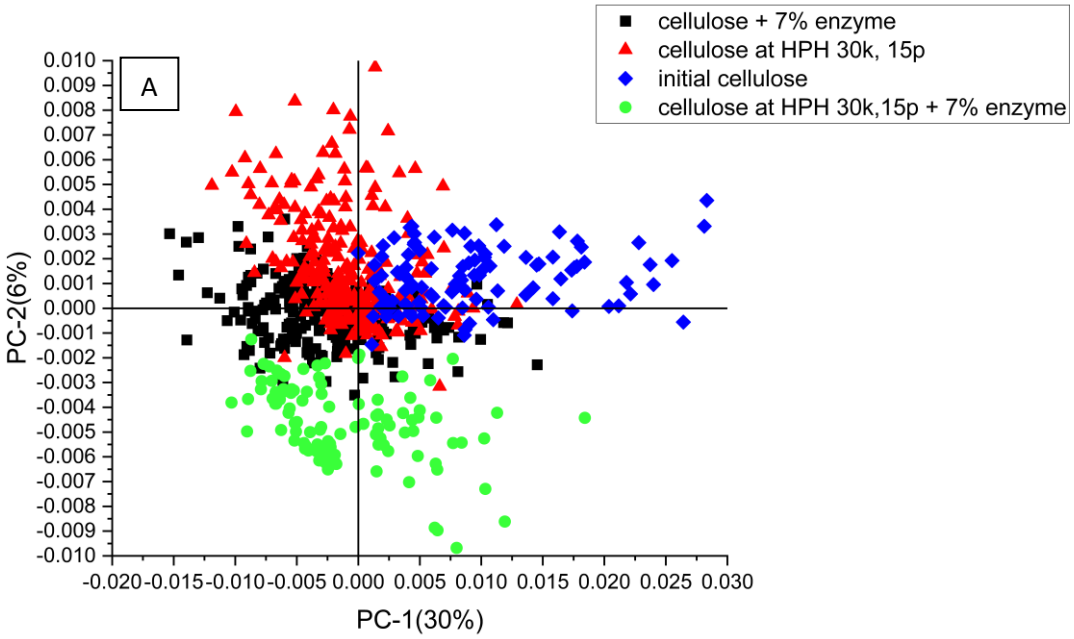
A
cellulose + 7% enzyme
cellulose at HPH 30k, 15p
initial cellulose
cellulose at HPH 30k,15p + 7% enzyme
PC-2(6%)
PC-1(30%)

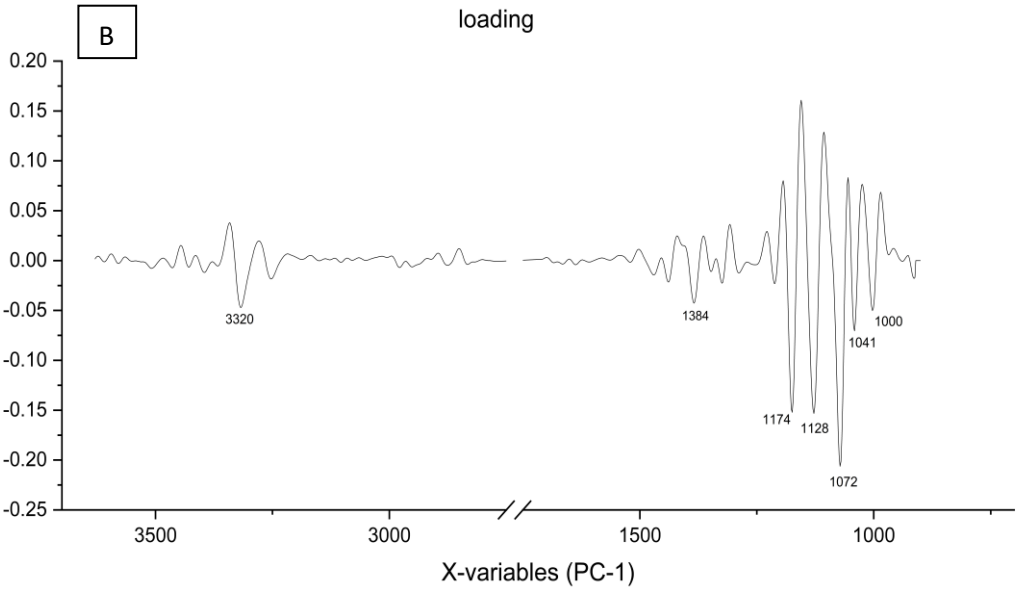
B
loading
3320
1384
1000
1041
1174
1128
1072
X-variables (PC-1)

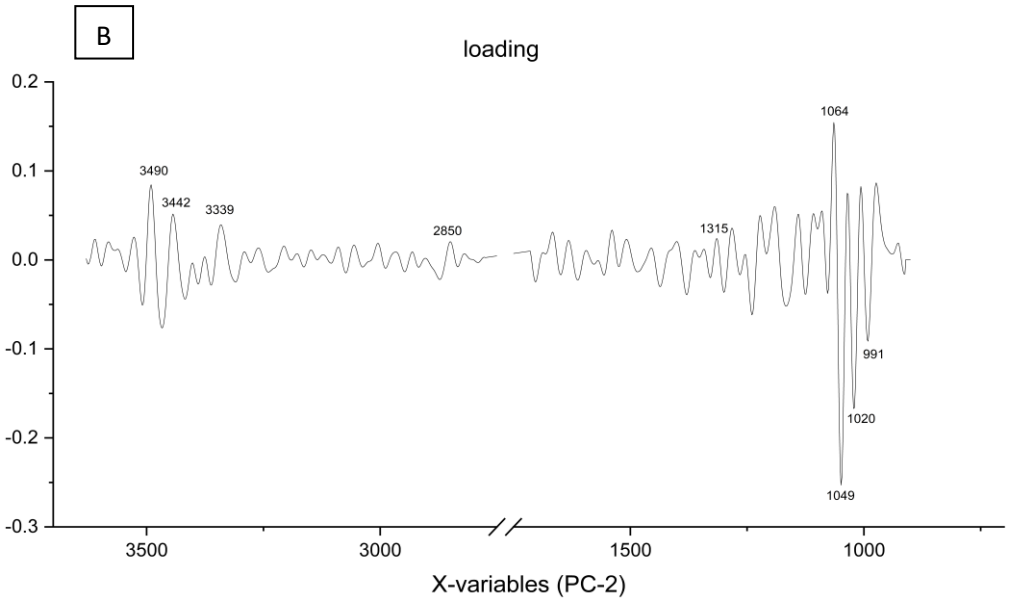

Figure 4.7 The principal component analysis (PCA) score plot of FTIR spectra Principal component analysis score plots (A) and loading plots (B) from 2nd derivative spectra of nanocellulose in different conditions and initial cellulose. Spectra derived using second-derivative processing with the entire biochemical fingerprint region (1800–900 cm^{-1}) and (3500–2800 cm^{-1}).

The second derivative analysis of designated spectral regions within the FTIR spectra, as depicted in Figure 4.8, the band around 3490 cm^{-1} and 3442 cm^{-1} was employed to comparatively assess the nanocellulose samples processed under various conditions with the pristine cellulose. The co-localized band observed at these wavenumbers corresponds to intramolecular hydrogen bonding within cellulose II (Hishikawa et al., 2017; Makarem et al., 2019), whereas the peak at 3339 cm^{-1} is characteristic of intramolecular hydrogen bonding in cellulose Iα and Iβ. The peak at 3276 cm^{-1} is attributed to intermolecular hydrogen bonding in cellulose Iβ. Both the mechanical processing and enzymatic hydrolysis treatments are known to augment the surface area of the cellulose particles, thereby exposing a greater number of hydroxyl (OH) groups. This phenomenon manifests as a more intense and well-defined peak at the OH stretching frequency within the FTIR spectra. The intensity of the intermolecular hydrogen bonding peak (3276 cm^{-1}) serves as an indicator of the crystallinity of cellulose. The observed enhancement in OH stretching intensity associated with intramolecular hydrogen bonding suggests a transformation of the crystalline structure towards a more

amorphous state following the combined application of mechanical and enzymatic treatments.

The band at 2919 cm^{-1} corresponds to CH stretching vibration, while the bands at 2852 cm^{-1} and 2965 cm^{-1} are assigned to CH_2 symmetric and asymmetric stretching vibrations in cellulose, respectively (Doumenq, 2019; Makarem et al., 2019). The presence of the band at 1511 cm^{-1}, attributed to aromatic skeletal vibration in lignin (Javier-Astete et al., 2021; Md Salim et al., 2021), suggests the efficacy of both delignification methods in disrupting the lignin structure.

The peaks at 1459 cm^{-1}, 1373 cm^{-1}, and 1315 cm^{-1} are associated with CH_2 bending vibration in crystalline cellulose I, while the peak at 1425 cm^{-1} corresponds to CH_2 asymmetric stretching vibration in amorphous cellulose (Doumenq, 2019; Makarem et al., 2019). The peak at 1278 cm^{-1} is attributed to CH deformation in both cellulose I and II. The peaks at 1162 cm^{-1} and 1120 cm^{-1} are indicative of C-O-C asymmetric stretching vibration in cellulose I and II (Kudzin et al., 2021; Doumenq, 2019; El Oudiani et al., 2017). Finally, the peaks at 1062 cm^{-1}, 1029 cm^{-1}, and 995 cm^{-1} are assigned to C-O vibration and C-O valence vibration in cellulose (Parihar et al., 2019; El Oudiani et al., 2017).

High-pressure homogenization alters the chemical architecture of cellulose by fragmenting the fibers into nanoscale particles. This process disrupts existing hydrogen bonds within the cellulose fibers and potentially facilitates the formation of new ones. The high pressure and shear forces can also induce mechanical stress, promoting the formation of novel hydrogen bonds between cellulose molecules, resulting in a more densely packed and organized structure. Enzymatic hydrolysis modifies the chemical structure by generating new chemical functionalities on the surface of the cellulose fibers as it cleaves the glycosidic bonds. These modifications can further influence the chemical composition of the resulting nanocellulose.

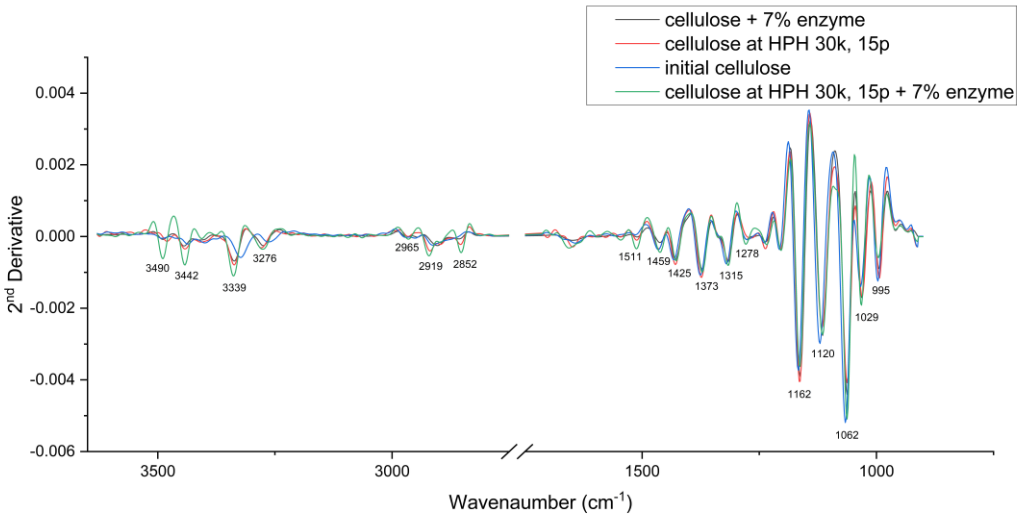

Figure 4.8 The average second derivative spectra obtained from FTIR spectra nanocellulose in different conditions and initial cellulose. The spectra after 13 points of smoothing and normalized with extended multiplicative signal correction over the range of 3630-2770 $cm^{-1}$and 1720-900 cm^{-1}.

4.1.4 WAXS analysis

Wide-angle X-ray scattering (WAXS) analysis is a well-established technique for characterizing crystalline structures. The WAXS patterns of the nanocellulose samples are presented in Figure 4.9. The characteristic scattering peaks for cellulose I were observed at 2θ = 14.8°, 16.3°, 20.6°, 22.4°, and 34.4° (Cheng et al., 2014), while those for cellulose II were identified at 2θ = 12.4°, 20.2°, and 21.8° (Cheng et al., 2014). The peaks at 2θ = 26.5° and 27.8° were attributed to natural graphite (Lionetto et al., 2019) and natural silver chloride (Chen et al., 2014), respectively. The unidentified peaks at 2θ = 36.4° and 39.2° could potentially originate from natural minerals present in the sample.

The crystallinity index (CI) of cellulose was determined using the WAXS deconvolution method implemented in SAXSIT software. This method involves separating the amorphous and crystalline contributions in the WAXS spectrum through curve fitting using Voigt functions. The resulting CI values are shown in Figure 4.10.

The initial cellulose exhibited a high CI of 59.2%. However, high-pressure homogenization led to a decrease in CI, possibly due to the disruption of the crystalline structure by the high-pressure forces. Conversely, enzymatic hydrolysis initially resulted in an increase in CI with increasing enzyme concentration up to 5%. However, CI

decreased to 50% when 7% enzyme was added. During homogenization, the mechanical forces can disrupt hydrogen bonding networks within cellulose crystalline domains (Nechyporchuk et al.,2016), the high shear forces and localized pressure differences randomly create structural defects in the crystalline regions, converting portions of crystalline cellulose to amorphous regions, and amorphous regions were destroyed, leading to the breakdown of the structure and size reduction.

For the enzymatic hydrolysis, the cellulase enzymes initially access and hydrolyze the more accessible amorphous regions (Siqueira et al., 2010, Peciulyte et al., 2015). The selective enzymatic hydrolysis preferentially attacks amorphous regions while leaving crystalline domains intact (Tata et al., 2015). This selective degradation effectively increases the proportion of crystalline material in the remaining cellulose. In another hand, higher enzyme loadings or extended reaction times, enzymes begin attacking the crystalline domains after depleting most accessible amorphous regions (Peng et al., 2015).Excessive enzymatic treatment can penetrate the ordered crystalline structure, creating defects and reducing overall crystallinity (Chen et al., 2016 , Park et al., 2010).

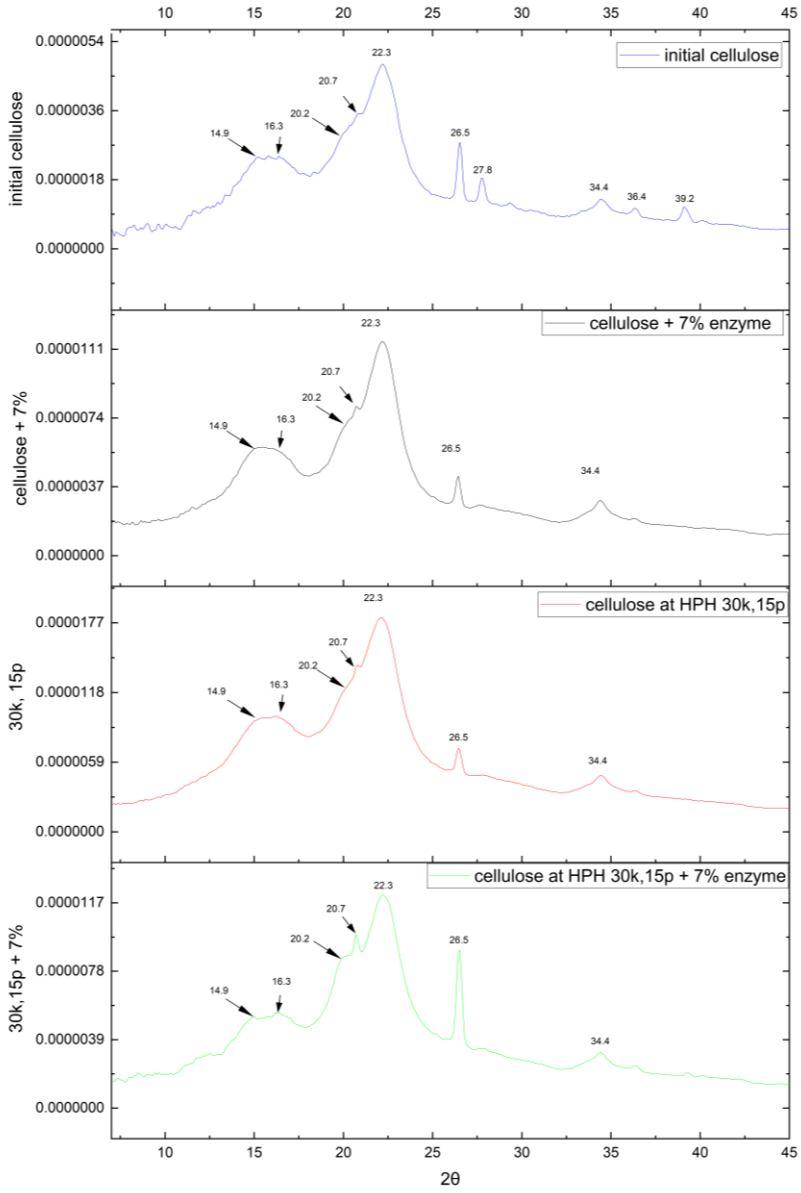

Figure 4.9 WAXS patterns of nanocellulose in different methods compared with initial cellulose.

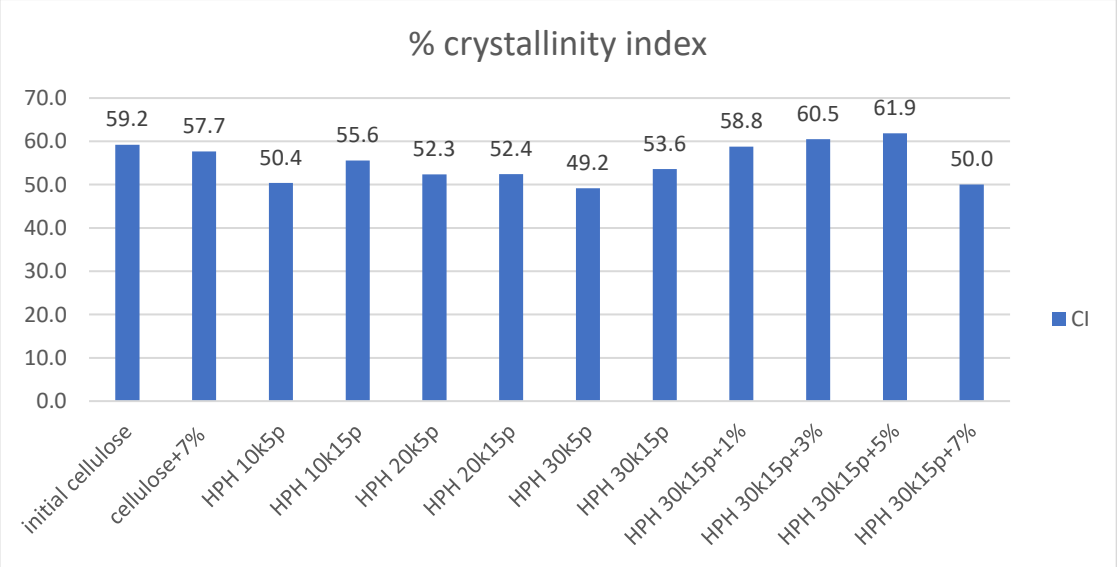

Figure 4.10 crystallinity index of cellulose in different methods.

4.2 Optimal scaffold production and scaffold characterization

4.2.1 Ratio optimization and analysis of scaffold

For the design of cell culture scaffolds, high hydrophilicity and absorption are crucial properties. These characteristics were evaluated by measuring the contact angles of water and cell culture media on the scaffolds. Additionally, the maximum tensile force was analyzed. Experiments were conducted according to the design outlined in Table 4.3, encompassing a total of 19 runs. The water contact angle, cell culture medium contact angle, and maximum tensile force for each run are presented in Table 4.3. To analyze the influence of factors and the relationships between variables, both analysis of variance (ANOVA) and Response Surface Methodology (RSM) were employed. Statistical values including sequential model sum of squares, adjusted coefficient of determination, predicted coefficient of determination, and lack of fit were assessed to determine the suitability of the model.

Table 4.3 mixture designed experiment and results of water contact angle, medium contact angle and maximum tensile force

Run	PLA(%)	PBS(%)	nanocellulose (%)	water contact angle(radius)	medium contact angle(radius)	average maximum tensile force(g)
1	77.50	17.50	5.00	73.29	79.76	1175.40
2	65.00	26.71	8.29	62.20	67.85	956.83
3	77.50	17.50	5.00	71.42	66.10	1175.40
4	65.00	26.71	8.29	64.36	61.43	956.83
5	90.00	7.11	2.89	60.79	60.69	1739.58
6	76.30	23.70	0.00	89.07	79.04	1344.92
7	90.00	7.11	2.89	69.87	62.17	1739.58
8	84.10	11.53	4.37	91.87	82.20	1649.75
9	77.50	17.50	5.00	73.86	73.44	1175.40
10	65.00	35.00	0.00	59.57	63.44	1456.92
11	82.62	7.38	10.00	82.21	74.42	1890.25
12	74.69	15.31	10.00	72.49	82.47	1203.28
13	82.53	17.47	0.00	83.12	82.37	1030.75
14	88.58	1.42	10.00	77.34	76.78	1640.72
15	70.14	28.99	0.87	72.60	62.43	1089.45
16	77.50	17.50	5.00	74.05	82.76	1175.40
17	82.53	17.47	0.00	98.34	113.72	1030.75
18	69.24	20.76	10.00	97.78	72.33	1330.40
19	88.58	1.42	10.00	77.23	76.38	1640.72

Statistical analysis was employed to select a model equation that effectively described the relationship between the water contact angle, maximum tensile force, and the composite material ratio of the cell culture scaffold. A quartic model exhibited the best fit for this relationship, whereas a quadratic model was more appropriate for the contact angle of the cell culture medium and the ratio.

The suitability of the model equations for explaining or predicting experimental outcomes was evaluated using several coefficients (presented in Table 4.4). These coefficients included the coefficient of determination (R^2), adjusted coefficient of determination (adj-R^2), predicted coefficient of determination (pred-R^2), and lack of fit (p-value).

The R^2 values for the water contact angle and maximum tensile force experiments were high (0.8772 and 0.9203, respectively). Generally, a higher R^2 value approaching unity indicates a stronger correlation between the model and the experimental data. In these instances, the close agreement between the model predictions and the experimental observations suggests that the model equations can be used for accurate explanation or prediction.

However, the R^2 value for the cell culture medium contact angle experiment was lower (0.5153), signifying a poor fit. This translates to a substantial discrepancy between the model predictions and the experimental results, thereby diminishing the model's accuracy for explanation and prediction in this context.

For a robust model, the adj-R^2 value should be close to the R^2 value, and a high pred-R^2 value indicates the model's efficacy in predicting response values for novel data points. However, all three experiments exhibited relatively low pred-R^2 values, suggesting that the models are not well-suited for predicting the response of new data.

Furthermore, an analysis of variance (ANOVA) was conducted, and the coefficient of variation (C.V.%) was examined. A lower C.V.% value signifies less variance in the data relative to the mean. The C.V.% values for the water contact angle and maximum tensile force experiments were relatively low (7.12% and 8.41%, respectively), indicating minimal data variation. Conversely, the cell culture medium contact angle experiment exhibited a higher C.V.%, suggesting greater data variance.

A statistically significant p-value for lack of fit indicates that the model inadequately describes the data. The p-values for lack of fit for the water contact angle and cell culture medium contact angle experiments were 0.2203 and 0.4320, respectively, suggesting that the lack of fit is not statistically significant in these cases. However, the p-value for lack of fit in the maximum tensile force experiment was not reported. It is essential to assess this value to definitively determine the model's suitability for this relationship.

Finally, the Water contact angle, The model fits well with a high R^2 and reasonable C.V. The predicted R^2 is low, indicating potential issues in generalizing to new data. Medium contact angle, the model shows moderate fit, but the predicted R^2 is very low, suggesting the model may not generalize well to new data. Maximum Tensile force, the model shows an excellent fit with high R^2 and relatively low C.V., but the low predicted R^2 suggests caution in generalizing the model.

Table 4.4 the data from ANOVA for fitted model

properties	fitted model	sequential P-value	P-value Lack of fit	R^2	adj-R^2	pred-R^2	C.V.(%)
water contact angle	special quartic quadratic	0.0046	0.2203	0.8772	0.779	0.2189	7.12
medium contact angle	quadratic linear	0.0347	0.432	0.5153	0.3288	0.0455	13.55
maximum tensile force	special quartic quadratic	0.0011	-	0.9203	0.8566	0.3237	8.41

Assessment of a model's suitability for variance prediction necessitates residual plot analysis to corroborate the predictions generated by the model equations. Commonly employed plots for this purpose include normal probability plots of residuals, residuals versus predicted values, and predicted versus actual values.

The residual plots for the water contact angle experiment were depicted in Figure 4.11. The data points in the normal probability plot (Figure 4.11A) exhibit a tight distribution around the regression line (red line), signifying minimal deviations from the mean. Similarly, the residuals in the residual versus predicted plot (Figure 4.11B) cluster around the zero line (black line) with no observations exceeding the control lines (red lines). This indicates a favorable distribution of data devoid of outliers. Finally, the predicted versus actual plot (Figure 4.11C) demonstrates that the data points concentrate around the diagonal line (black line), suggesting low errors relative to the predicted

values. Based on this residual analysis, the model appears well-suited for predicting the water contact angle.

However, the residual plots for the cell culture medium contact angle (Figure 4.12) and maximum tensile force (Figure 4.13) experiments reveal some limitations. In the normal probability plots (Figures 4.12A and 4.13A), certain data points (circled) deviate considerably from the regression line, indicating substantial deviations from the mean. Furthermore, while most data points in the residual versus predicted plots (Figures 4.12B and 4.13B) cluster near the zero line, a solitary circled data point falls outside the control lines, suggesting the presence of an outlier. Although most data points in the predicted versus actual plots (Figures 4.12C and 4.13C) lie close to the diagonal line, the circled data points exhibit significant errors compared to the predicted values.

These observations gleaned from the residual plots for the cell culture medium contact angle and maximum tensile force experiments suggest potential shortcomings in the model's capacity to predict these outcomes. While the elimination of outlying data points might seem appealing, a critical investigation into the underlying causes of these deviations is paramount. Re-analyzing the data after addressing these issues might enhance the model's predictive capability.

A)

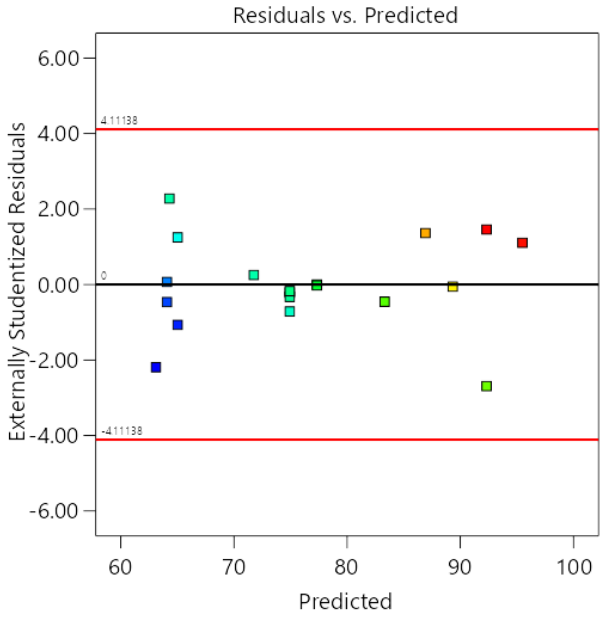
Residuals vs. Predicted
Externally Studentized Residuals
Predicted
6.00
4.00
2.00
0.00
-2.00
-4.00
-6.00
4.11138
0
-4.11138
60
70
80
90
100

.

B)

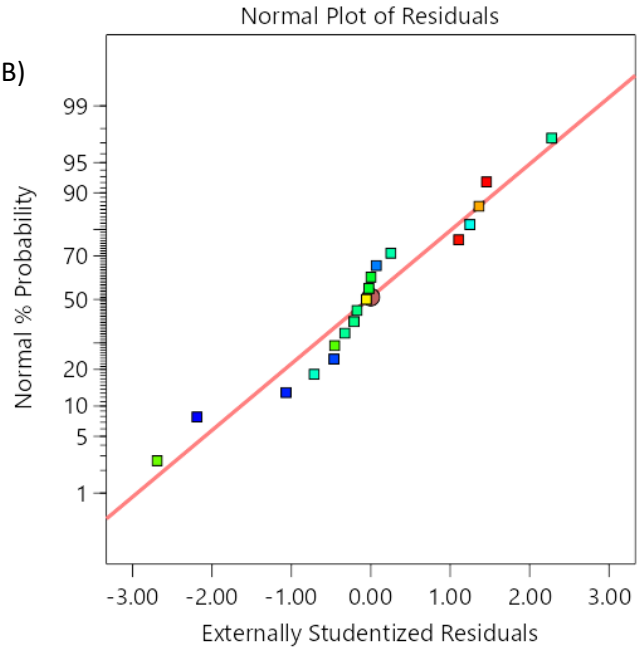
Normal Plot of Residuals
Normal % Probability
Externally Studentized Residuals
99
95
90
70
50
20
10
5
1
-3.00
-2.00
-1.00
0.00
1.00
2.00
3.00

C)

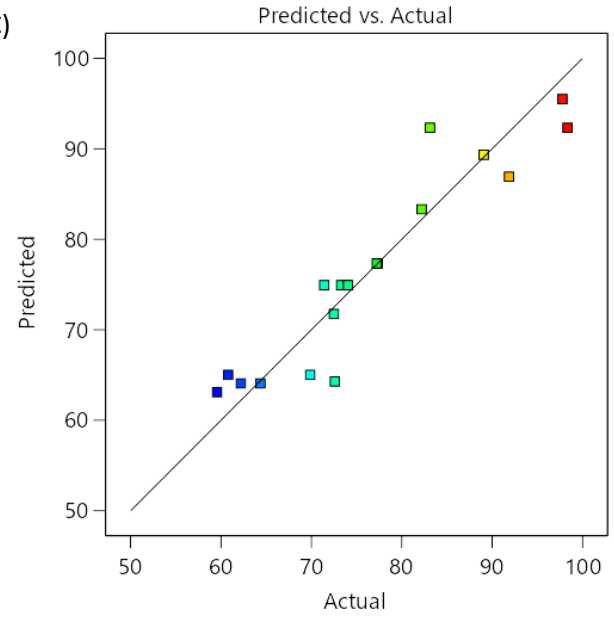

Figure 4.11 verification of the model of the water contact angle experiment : A) Normal plot of Residual, B) Residual Vs. Predicted, C) Predicted Vs. Actual

A)

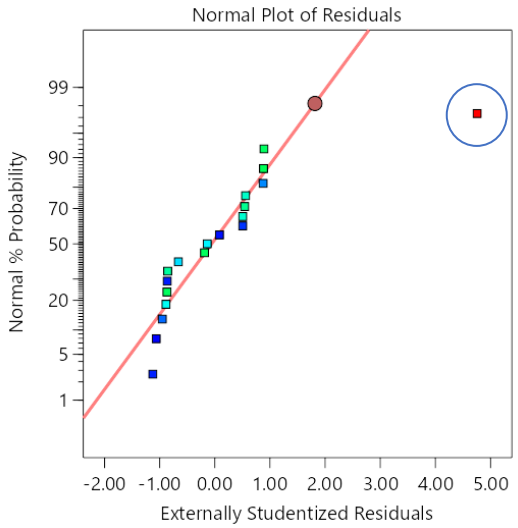

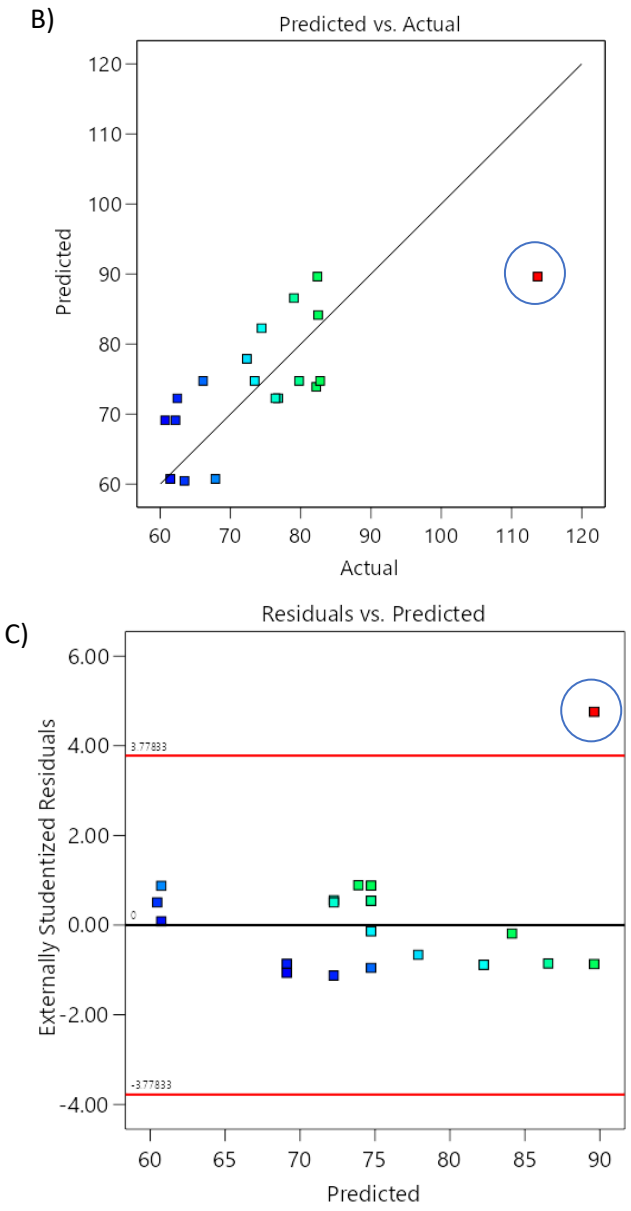

Figure 4.12 verification of the model of the cell culture medium contact angle experiment : A) Normal plot of Residual, B) Residual Vs. Predicted, C) Predicted Vs. Actual

A)

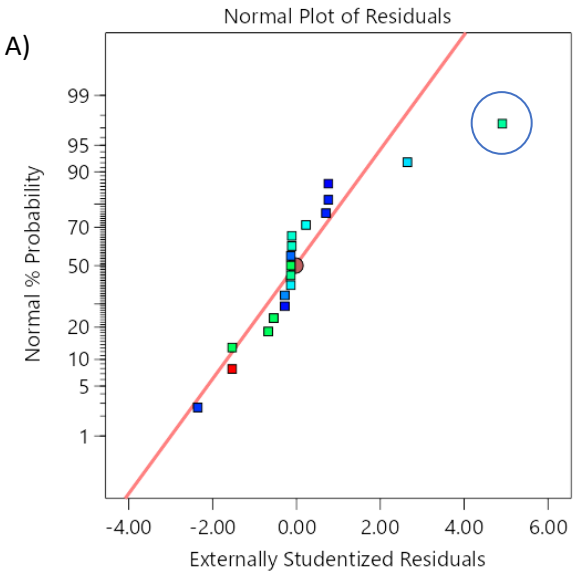
Normal Plot of Residuals
Normal % Probability
99
95
90
70
50
20
10
5
1
-4.00
-2.00
0.00
2.00
4.00
6.00
Externally Studentized Residuals

B)

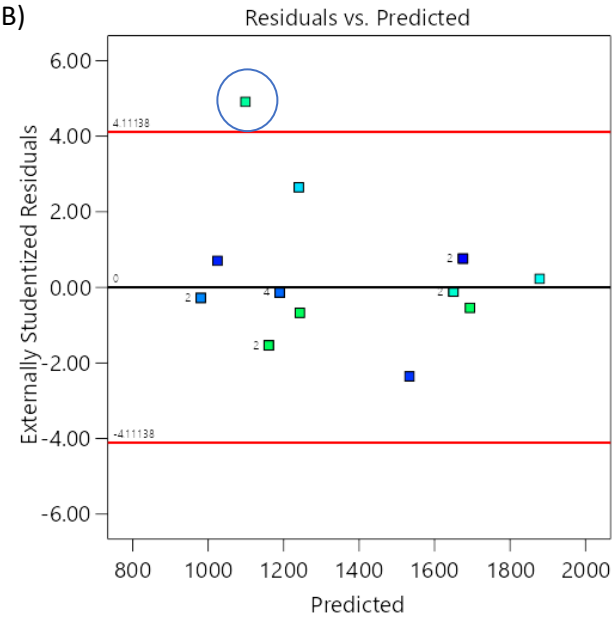
Residuals vs. Predicted
Externally Studentized Residuals
6.00
4.00
2.00
0.00
-2.00
-4.00
-6.00
4.11138
-4.11138
800
1000
1200
1400
1600
1800
2000
Predicted

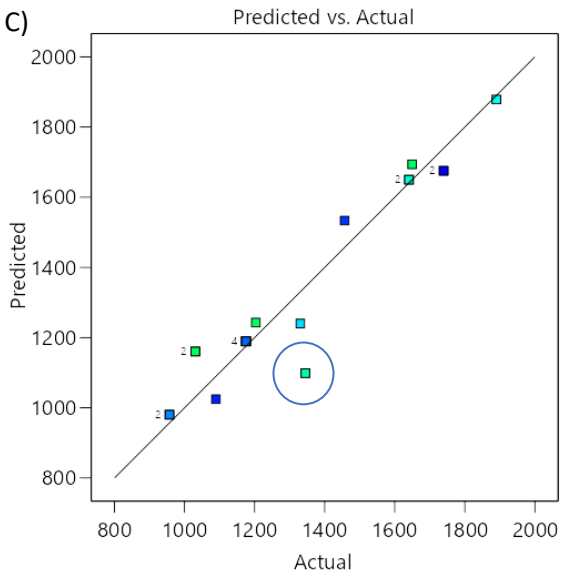

Figure 4.13 verification of the model of the maximum tensile force experiment : A) Normal plot of Residual, B) Residual Vs. Predicted, C) Predicted Vs. Actual

Response Surface Methodology (RSM) constitutes a statistical approach for optimizing production processes. It achieves this by generating a mathematical model that elucidates the interactions between various experimental variables. RSM can be employed to visually represent the relationships between variables through contour plots. Figure 4.14 exemplifies this concept. Within these plots, red areas signify the highest observed values, yellow and green areas represent intermediate values, and blue areas depict the lowest values.

In the water contact angle experiment, the red area is localized within the region of high PLA concentration. This observation implies that PLA addition leads to an increase in the water contact angle of the scaffold, which translates to a reduction in material hydrophilicity. Conversely, the incorporation of PBS and nanocellulose appears to enhance the hydrophilicity of the material.

The cell culture medium contact angle experiment, as illustrated in Figure 16B, exhibits trends analogous to those observed in the water contact angle experiment. In this case, the maximum tensile force demonstrates an increase with the addition of both PLA and nanocellulose, but exhibits a decrease with the addition of PBS.

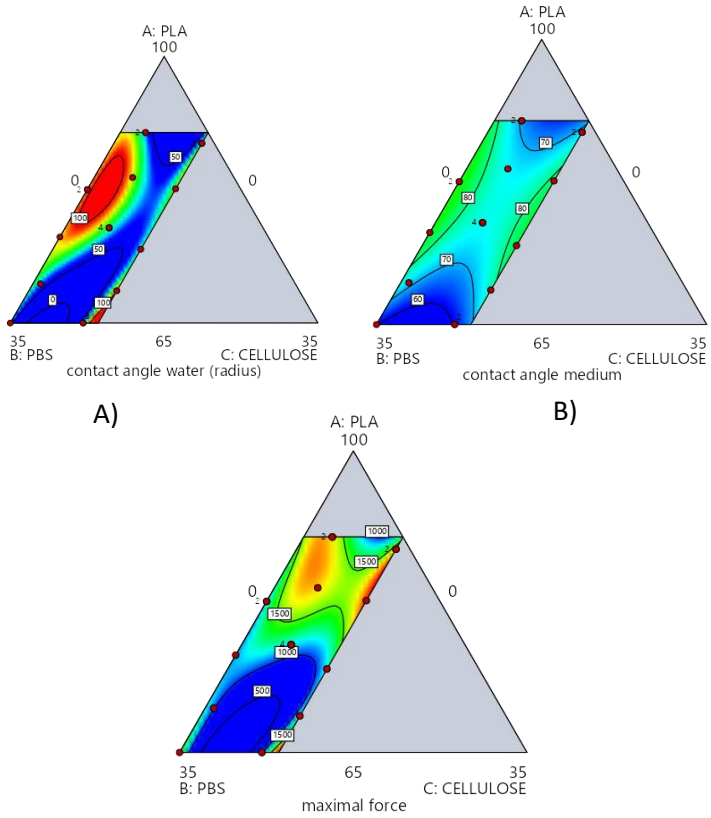

Figure 4.14 Contour plot obtained after optimization (RSM): A) contact angle of water, B) contact angle of cell culture medium and C) maximum tensile force

Response Surface Methodology (RSM) was implemented to optimize the ratio of composite materials under the following constraints, PLA content: 65% to 90% (65% ≤ PLA ≤ 90%), PBS content: maximum 35% (PBS ≤ 35%), Nanocellulose content: maximum 10% (nanocellulose ≤ 10%), Combined PBS and nanocellulose content: maximum 40% (PBS + nanocellulose ≤ 40%), Total content of 100% (PLA + PBS + nanocellulose = 100%)

Analysis via RSM revealed the optimal ratio for cell culture scaffold production to be 65% PLA, 26.814% PBS, and 8.186% nanocellulose. Subsequently, this ratio was validated through the fabrication of cell culture scaffolds with the aforementioned composition. The fabricated scaffolds were then subjected to characterization for water contact angle, cell culture medium contact angle, and maximum tensile force to corroborate their suitability.

As depicted in Figure 4.15, the water contact angle and cell culture medium contact angle of the scaffolds produced under the optimal conditions were 67.72 degrees and 65.61 degrees, respectively. Furthermore, the maximum tensile force was measured to be 651.425 g.

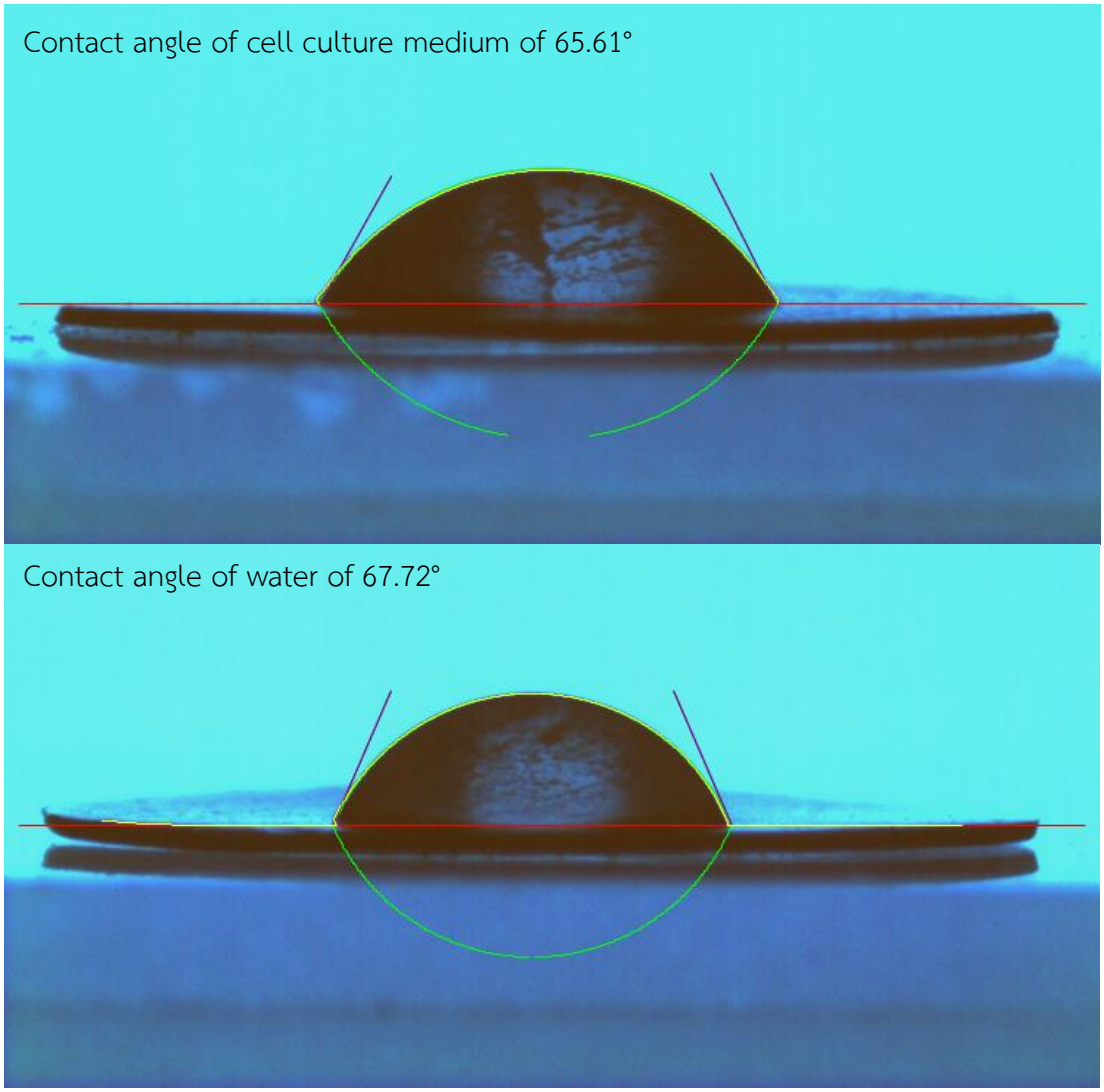

Figure 4.15 contact angle images of cell culture medium (up) and water (bottom) on optimal scaffold

4.2.2 Thermal stability analysis

Thermogravimetric analysis (TGA) was employed to investigate the thermal degradation profiles of nanocellulose, PLA, PBS, PLA/PBS and the composite scaffold, as illustrated in Figure 4.16. The TGA results for nanocellulose exhibited a two-stage weight

loss pattern. The initial stage, likely attributable to the decomposition of inherent natural components, occurred at approximately 180 °C. Notably, the final decomposition temperature of nanocellulose yielded the highest residual weight (29.64%) compared to the other materials. Conversely, the residual weights of PLA, PBS, PLA/PBS, and the scaffold were 10.67%, 6.26%, 1.59%, and 1.57%, respectively. Nanocellulose retains the highest residual weight (29.64%), indicating superior thermal stability due to its crystalline structure and the formation of carbonaceous residues that resist further degradation. In contrast, PLA (10.67%) and PBS (6.26%) decompose more extensively, with PBS exhibiting lower thermal stability than PLA. The PLA/PBS blend (1.59%) and the scaffold (1.57%) show the lowest residual weights, This suggests potential interactions between materials in the blend that may reduce overall thermal stability. The high biodegradability of PLA/PBS and the scaffold is advantageous for biomedical applications such as tissue engineering, where controlled degradation supports tissue regeneration.

Table 4.5 summarizes the critical parameters associated with thermal stability, including the onset decomposition temperature, the peak decomposition temperature, and the final decomposition temperature. It is noteworthy that the thermal degradation of the scaffold exhibited a decrease relative to the individual components. This observation suggests that the blending process might have induced a chemical restructuring within the composite materials.

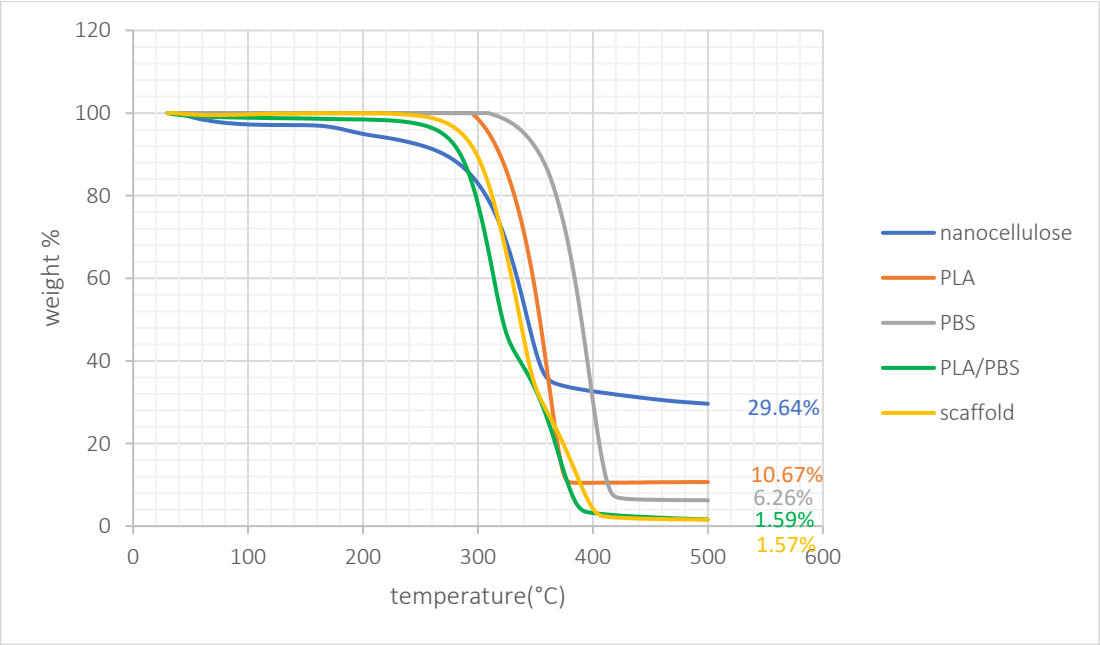

Figure 4.16 weight loss of nanocellulose, PLA, PBS and scaffold (PLA 65%, PBS 26.82%, nanocellulose 8.18%) at temperature of 20 ℃ to 500 ℃

Table 4.5 TGA results of nanocellulose, PLA, PBS and scaffold (PLA 65%, PBS 26.82%, nanocellulose 8.18%)

sample	Starting decomposition temperature	Maximum decomposition temperature	Ending decomposition temperature
nanocellulose	290	340	381
PLA	297	359	390
PBS	320	376	427
PLA/PBS	260	311	409
Scaffold	260	334	415

4.2.3 Thermal properties analysis

Differential scanning calorimetry (DSC) analysis was employed to investigate the thermal properties of PLA, PBS, nanocellulose, and the composite scaffold. The findings, as depicted in Figure 4.17 and summarized in Table 4.6, provide valuable insights into the material behavior of the scaffold.

The DSC thermogram of the nanocellulose revealed a distinct endothermic peak at 187.6 °C, attributable to the evaporation of inherent moisture content. Interestingly, the glass transition temperature (Tg) and melting temperature (Tm) of the PLA fraction exhibited a slight reduction within both the PLA/PBS blend and the composite scaffold compared to pure PLA. The PLA/PBS blend displayed a Tg peak at approximately 64.7 °C and a Tm peak at 149.5 °C. The scaffold exhibited a Tg peak of around 62.3 °C and a Tm peak of 150.4 °C. Notably, the PBS fraction within both the blend and the scaffold displayed distinct Tm peaks at 113.9 °C and 111.7 °C, respectively.

Furthermore, the crystallinity of both the PLA and PBS fractions within the scaffold displayed an enhancement with the incorporation of nanocellulose. This observation suggests that nanocellulose may facilitate the rearrangement of ordered PLA and PBS molecular chains during the blending process. In this context, nanocellulose can be considered analogous to a nucleating agent, acting to promote the crystallization process within the composite scaffold.

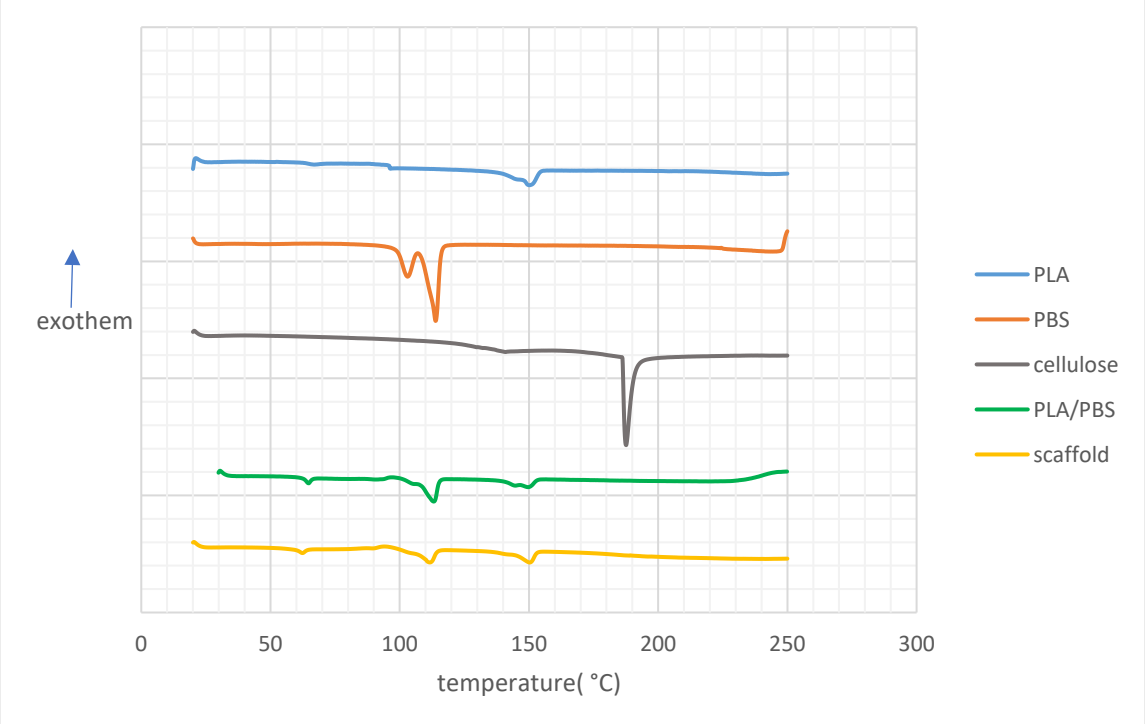

Figure 4.17 DSC results of nanocellulose, PLA, PBS PLA/PBS (PLA 60%, PBS 40%) and scaffold (PLA 65%, PBS 26.82%, nanocellulose 8.18%)

Table 4.6 DSC results of nanocellulose, PLA, PBS, PLA/PBS (PLA 60%, PBS 40%) and scaffold (PLA 65%, PBS 26.82%, nanocellulose 8.18%)

samples	PLA fraction				PBS fraction			
	T_g(°C)	T_m(°C)	H_m (J/g)	X_c(%)	T_g(°C)	T_m(°C)	H_m (J/g)	X_c(%)
PLA	67.1	150.4	31.88	34.27	-	-	-	-
PBS	-	-	-	-	-	113.9	129.3	64.65
PLA/PBS	64.7	149.5	16.23	29.09	-	113.9	37.45	46.81
Scaffold	62.3	150.4	19.87	32.87	-	111.7	27.04	50.41

4.2.4 Morphological analysis

Field-emission scanning electron microscopy (FESEM) was employed to investigate the morphological features of the surface of the nanocellulose-based biopolymer scaffold (comprised of 65 wt% PLA, 26.82 wt% PBS, and 8.18 wt% nanocellulose). The FESEM image, presented in Figure 4.18, depicts a surface topography characterized by abundant miniature pores and a striated texture. The presence of these pores suggests that the scaffold possesses a porous microstructure, which is a crucial characteristic for applications in tissue engineering, as it facilitates cell adhesion, proliferation, and nutrient transport (Lutzweiler et al., 2020). The striated texture observed on the surface may be attributed to phase separation between PLA and PBS, as these polymers have different miscibility and crystallization behaviors (Jompang et al., 2013). The incorporation of nanocellulose likely influences surface morphology by acting as a nucleating agent, leading to the formation of a more structured and interconnected network.

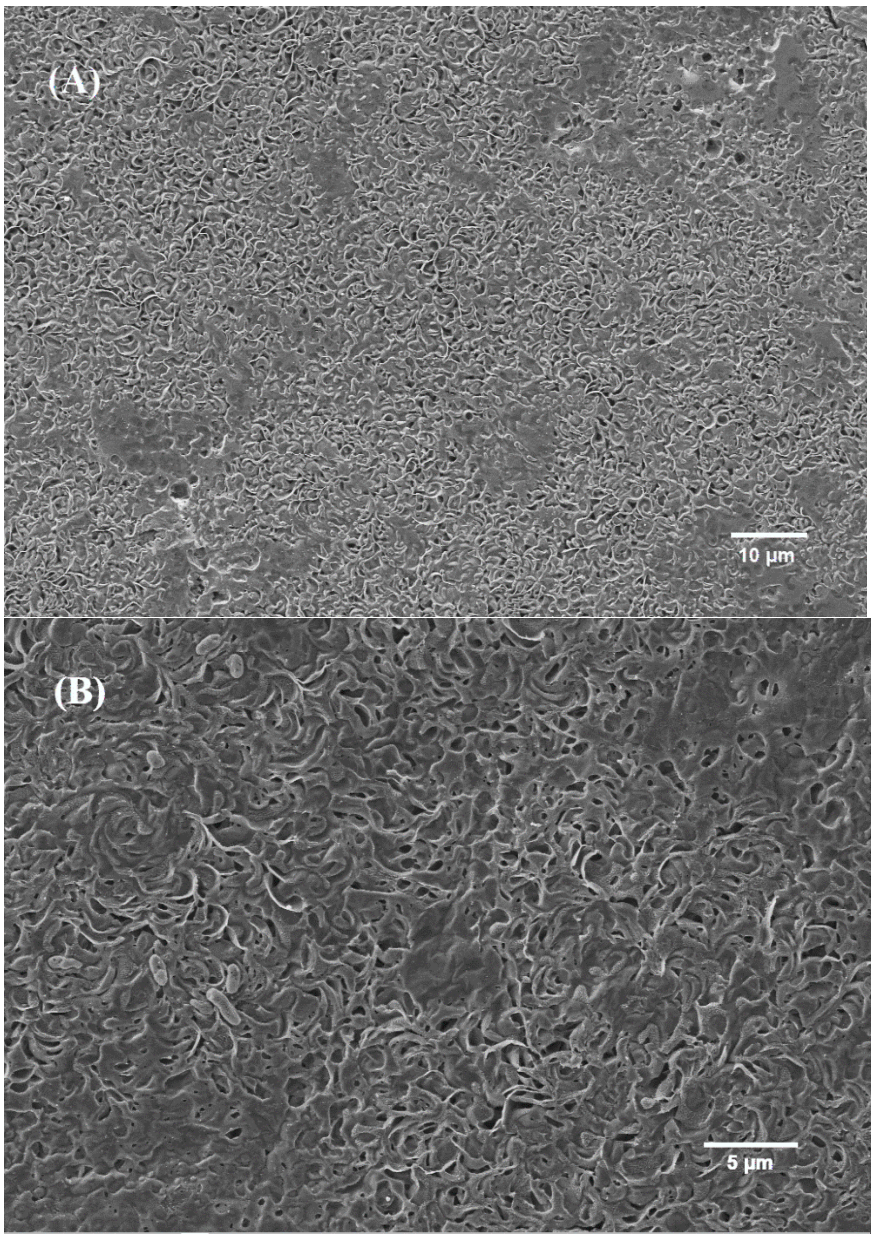
(A)
10 µm
(B)
5 µm

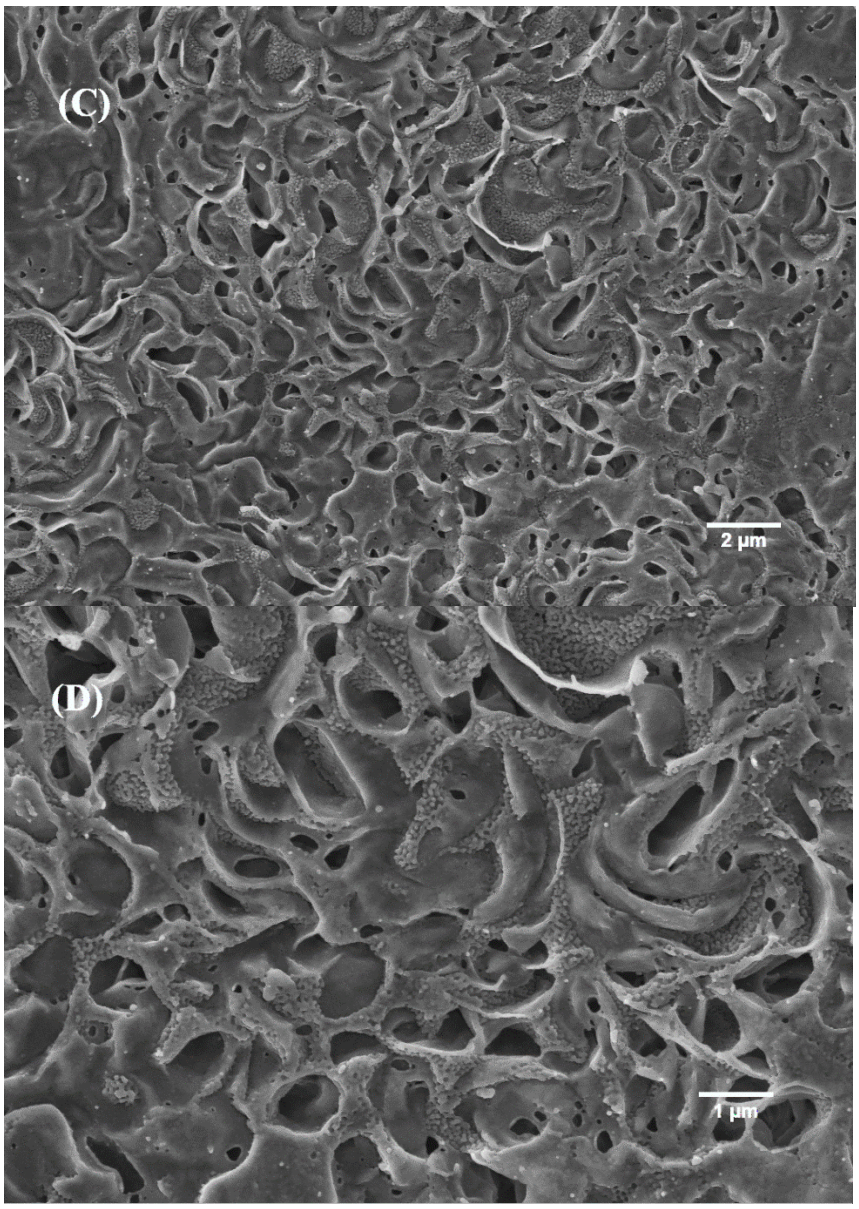
(C)
2 µm
(D)
1 µm

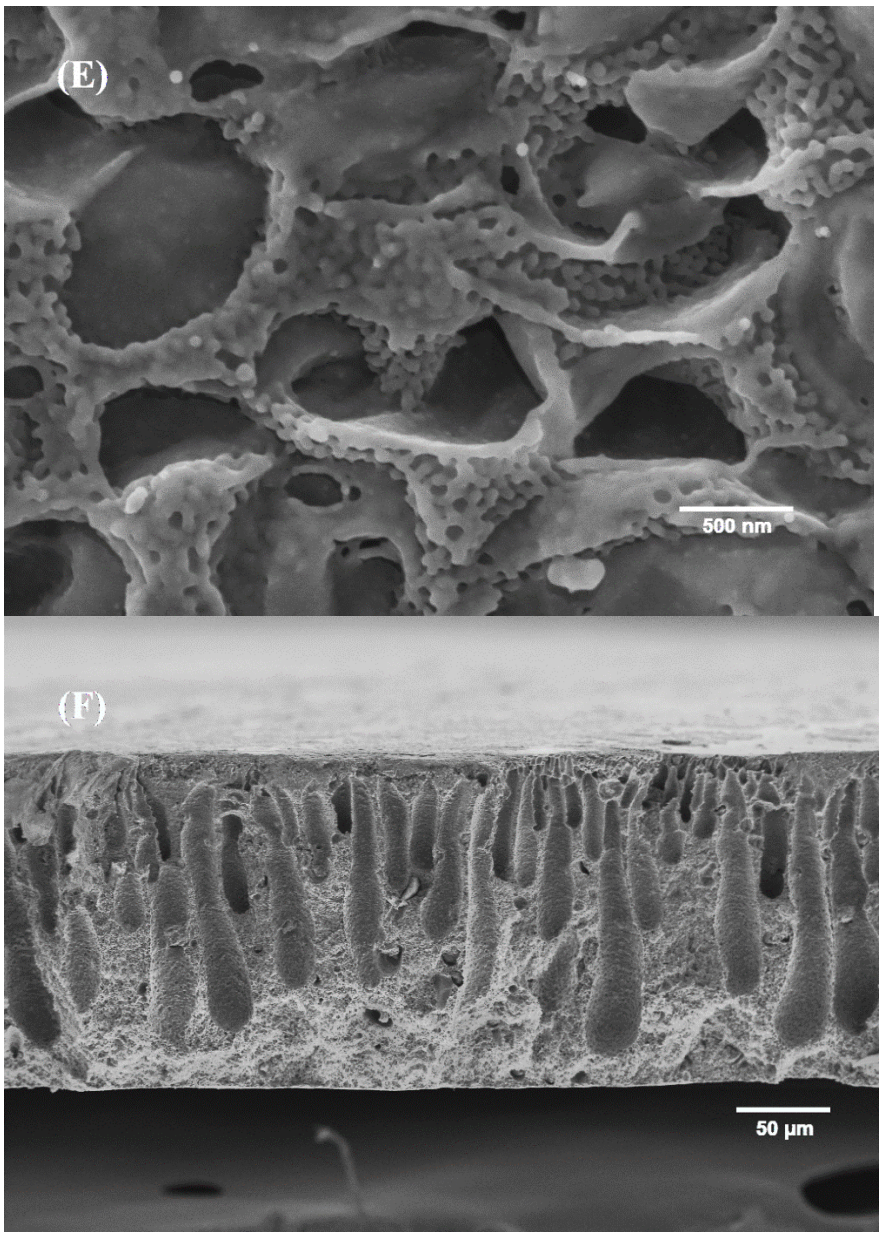

Figure 4.18 morphology of surface structure of nanocellulose based biopolymer scaffold (65% of PLA, 26.82% of PBS and 8.18% of nanocellulose) under FESEM : (A) scale bar of 10 µm, (B) scale bar of 5 µm, (C) scale bar of 2 µm, (D) scale bar of 1 µm (E) scale bar of 500 nm, and (F) cross-sectional area of scaffold, scale of 50 µm.

4.3 Cell culture analysis

4.3.1 Mesenchymal stem cells(hWJ-MSCs) viability on scaffold

An in vitro cytotoxicity evaluation of the scaffold was conducted. Human Wharton's Jelly Mesenchymal Stem Cells (hWJ-MSCs) were co-cultured with the scaffold

material within a complete medium for 72 hours. Subsequently, cell viability was quantitatively assessed using the MTT assay. The experiment was performed in triplicate to ensure data reproducibility. The analysis revealed an average cell viability of 96.65%.

4.3.2 Hepatogenic differentiation of hWJ-MSCs

The process of hepatogenic differentiation in hWJ-MSCs was evaluated microscopically on days 3, 6, 8, 10, 13, 15, and 17 as shown in figure 4.19. Light microscopy observations revealed morphological alterations indicative of hWJ-MSCs transitioning towards a hepatocyte-like morphology. Specifically, no substantial changes in cellular morphology were observed on days 3 and 6. However, on day 8, the cells commenced exhibiting shape transformations, which progressively continued towards the acquisition of a polygonal morphology by day 17.

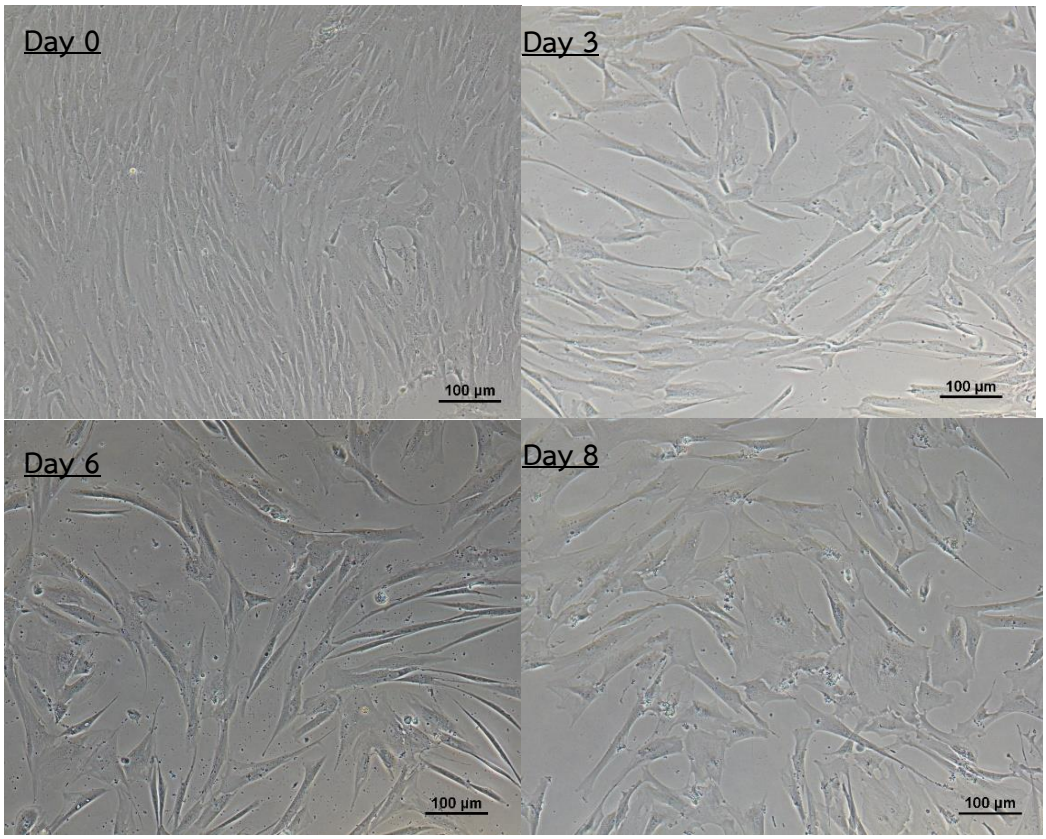

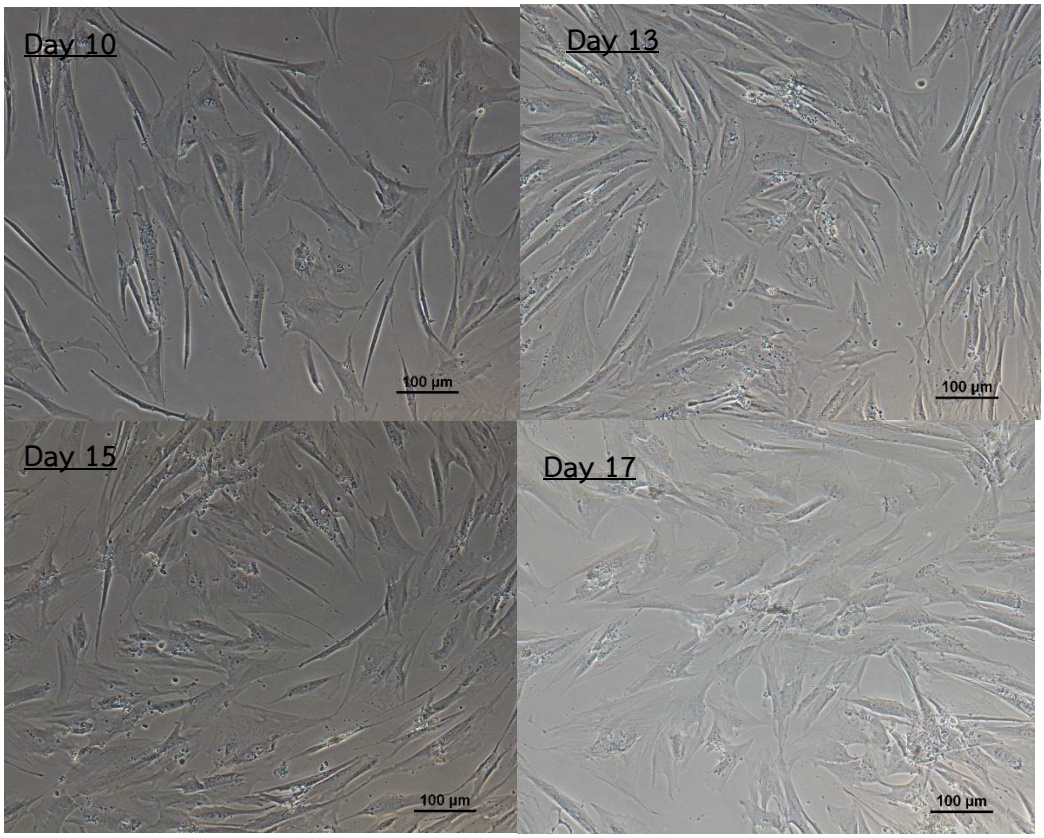

Figure 4.19 morphological change of Hepatogenic differentiation of Human Wharton's jelly – derived mesenchymal stem cells(hWJ-MSCs) for 17 days, scale bar of 100 µm.

4.3.3 Hepatogenic differentiation of Human Wharton's jelly – derived mesenchymal stem cells (hWJ-MSCs) on scaffold

Human Wharton's Jelly Mesenchymal Stem Cells (hWJ-MSCs) were seeded onto the scaffold as shown in Figure 4.20 (upper) to promote their differentiation towards a hepatocyte lineage. The findings, depicted in Figure 4.20 (bottom), corroborate the successful differentiation of hWJ-MSCs into hepatocyte-like cells on the aforementioned nanocellulose-based biopolymer scaffold (comprised of 65 wt% PLA, 26.82 wt% PBS, and 8.18 wt% nanocellulose).

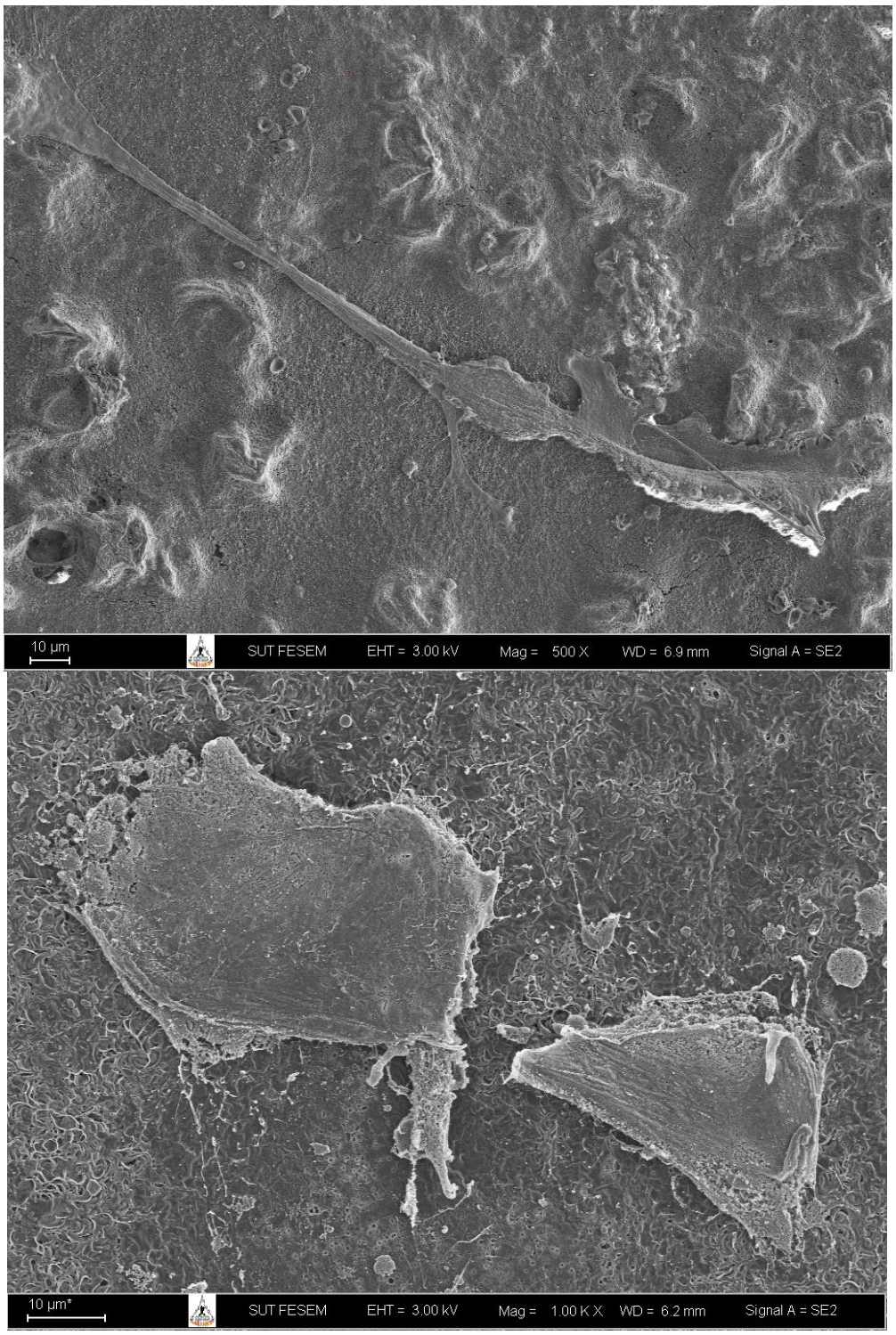

Figure 4.20 FESEM image of Human Wharton's jelly – derived mesenchymal stem cells (hWJ-MSCs) on nanocellulose based biopolymer scaffold (upper) and FESEM image of hepatocyte on nanocellulose based biopolymer scaffold (bottom), Human Wharton's jelly – derived mesenchymal stem cells (hWJ-MSCs) were induced into hepatocyte on scaffold using modified protocol for 17 days.

4.3.4 Immunofluorescence staining

The expression of hepatic markers (AFP, CK18, and ALB) in hepatogenic differentiated cells was investigated. Immunocytochemical analysis of hWJ-MSCs differentiated on the scaffold for hepatic lineage revealed the presence of all three hepatic markers as shown in figure 4.21. This finding supports the successful differentiation of hWJ-MSCs towards a hepatocyte-like phenotype on the scaffold.

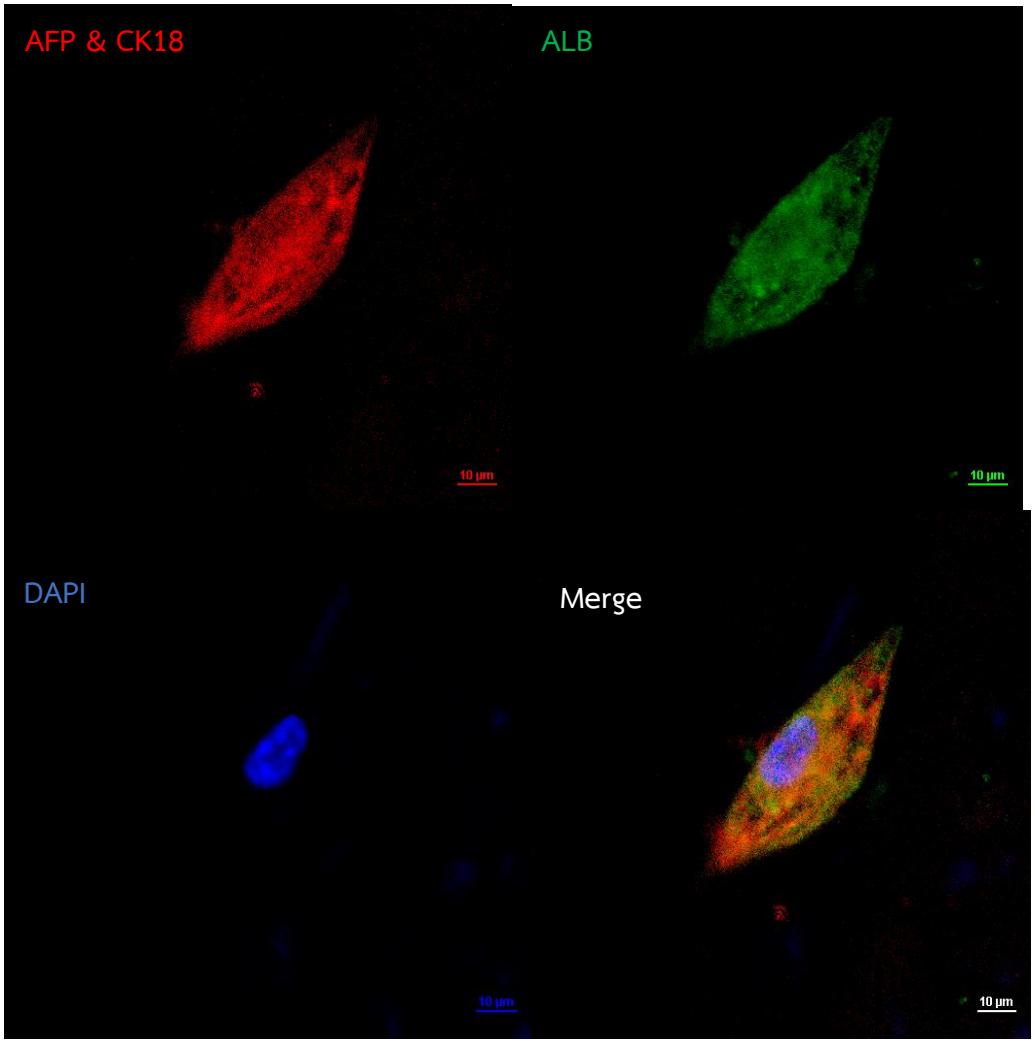

Figure 4.21 immunofluorescence analysis, AFP, CK18 = red, ALB = green and DAPI = blue; nucleus, scale bar = 10 µm.